BABES-BOLYAI UNIVERSITY

FACULTY OF PHYSICS

Interdisciplinary Research Institute on Bio-Nano-Sciences

Nanostructured phases of biomedical interest developed in sol-gel derived systems

PhD Thesis Summary

PhD student

Liliana Pătcaș

Scientific supervisor

Prof. Dr. Viorica SIMON

Cluj-Napoca

2015

Content

Key words: biomaterials, hyperthermia, radiotherapy, sol-gel method, thermal treatment, porosity, cancer, magnetic nanoparticles, bioactivity

Introduction

Biomaterials play a primary role in regenerative medicine aiming to restore and replace lost or dysfunctional tissues. Biomaterials as scaffolds serve for guiding temporary formation and organization of new tissue. In most cases it is necessary that the material used as scaffold to mimic as well as possible the characteristics of the extracellular matrix and to induce nano-scale natural processes of development and/or regeneration of tissue for healing applications.

Nanostructured biomaterials that mimic the extracellular matrix have shown the ability to actively regulate cellular responses including attachment, proliferation, differentiation and matrix formation [1]. Moreover, these nanostructured systems, if porous, can be loaded with appropriate medication for tissue regeneration, making it very interesting and intensively studied for a large range of applications in regenerative medicine.

Tissue regeneration depends on the successful interaction between cells and biomaterials, and in order to be successful in regenerative technologies the fundamental understanding of both life sciences and materials science is necessary. Based on the advantages of nanotechnologies, large progress has been made in biomaterials science. Various biomaterials have been developed which include nanofibers, nanocrystals, nanopores, nanospheres or other nanoscaled components..

Nanostructured biomaterials bring new solutions and their research in regenerative medicine is very attractive and largely investigated in order to obtain systems with physical, chemical, structural and biological properties adequate for biomedical applications. Of course, the nanostructured biomaterials are not limited to hard tissue regeneration, but they may be considered also for applications in soft tissue regeneration.

According to the literature [3], the bioactivity of silicate glasses and ceramics is based on a mechanism that begins with a dynamic ion release and uptake on biomaterial surface, when silanol groups (Si-OH) are formed, then a silica gel layer interacting with Ca^{2+} and PO_4^{3-} ions of the biological fluid.

It was also shown that bioactive glasses can promote gene expression in both hard tissue and soft tissue restoration and new glass systems were developed, a special attention being paid to their surface properties [4]. The compositions of these systems can be tailored according to specific applications. These include systems containing stable isotopes which can be activated by neutron irradiation. This is also the case of alumino-silicate glass particles containing yttrium, dysprosium, holmium, samarium, etc. which ca be radioactivated by neutron

irradiation and further used for in situ radiotherapy. Unlike the irradiation with external beam, the radiotherapy in situ protects the healthy surrounding the target malignant tissue [5]. At the same time, it has been shown experimentally that in certain ceramic systems magnetic crystalline phase may be developed which by hysteresis may provide local heating of tumor tissue, and can thus be considered for additional hyperthermia therapy [6-8]. The internal irradiation combined with local heating brings synergistic effects in cancer treatment [9]. For this reason new systems are searched to fulfill both conditions [10, 11].

In this thesis, new sol-gel derived bioactive glass systems with nanostructured phases of biomedical interest are studied, in view of their potential applications in cancer therapy by simultaneous in situ irradiation and hyperthermia.

Cap. III. Experimental results

1.Samples synthesis

The composition (in mol%) of the investigated ssystems was:

1. $50SiO_2 \cdot 30CaO \cdot 10Fe_2O_3 \cdot 10\ Dy_2O_3$
2. $50SiO_2 \cdot 28CaO \cdot 10Fe_2O_3 \cdot 10\ Dy_2O_3 \cdot 2ZnO$.

The two systems are further noted as SiCaFeDy and SiCaFeDyZn.

SiO_2 and CaO are the main glass network former and modifier, respectively, and both vigurously influence the bioactivity of calco-silicate glasses [2, 20]

Fe_2O_3·usually acts as network modifier and was introduced to form magnetic nanocrystalline phases considered for medical applications by hyperthermia therapy. The addition of Dy_2O_3 had in view the possibility to activate the stable isotope 164 of dysprosium, by irradiation with thermal neutrons, to the radioactive isotope 165, according to the reaction 164Dy**(n,γ)**165Dy. The radioisotope ^{165}Dy is a beta-emitter, with half-life of 2.3 hours, with mean free path of 1,9 mm and maximum penetration of 5,8 mm in soft tissues, eliberating an energy of E_β = 1.89 MeV [21]. The samples would be irradiated by thermal neutrons shortly before radiotherapy, in order to avoid as much as possible the non-medical exposure to radiation.

Zinc is nontoxic, chemically stable but flexible in terms of stereochemical, and because of amphoteric properties it can crucially influence the life processes involving zinc combinations In addition, zinc accelerates the bone healing processes, reduces the bone resorption and as introduced in bioglasses or a bioceramics it contributes to the improvement of their osteoinductive properties [24, 25, 82]. When ZnFe2O4 crystalline phase is formed, it can contribute as zinc ferrite for hyperthermia [26, 27].

The investigated $50SiO_2 \cdot 30CaO \cdot 10Fe_2O_3 \cdot 10\ Dy_2O_3$ and $50SiO_2 \cdot 28CaO \cdot 10Fe_2O_3 \cdot 10\ Dy_2O_3 \cdot 2ZnO$ systems were synthesised by sol–gel method (Fig. III.1) using as starting materials tetraethyl orthosilicate (TEOS, $Si(C_2H_5O)_4$, Sigma Aldrich), calcium nitrate ($Ca(NO_3)_2 \cdot 4H_2O$), iron nitrate ($Fe(NO_3)_3 \cdot 9H_2O$), dysprosium nitrate ($Dy(NO_3)_3 \cdot H_2O$) and respectively zinc nitrate hexahydrate ($Zn(NO_3)_2 \cdot 6H_2O$) with high grade of purity (99.9%). The sol was prepared by stirring TEOS with water and alcohol in a 1:2:1 weight ratio catalysed by HNO_3 and heated to 80 ºC for about 30 min in a closed recipient in order to achieve a complete hydrolysis. Sol–gel method, via hydrolysis and condensation of molecular

precursors, was considered due to this is a high-purity process that leads to excellent homogeneity. After the gel formation, the samples were dried in an electric oven at 110 °C for 24 h and then heat-treated at 800 °C and at 1200 °C for 3 h respectively, according to DTA measurements. The aim of the thermal treatment was to facilitate the growth of magnetic iron oxide crystalline phases.

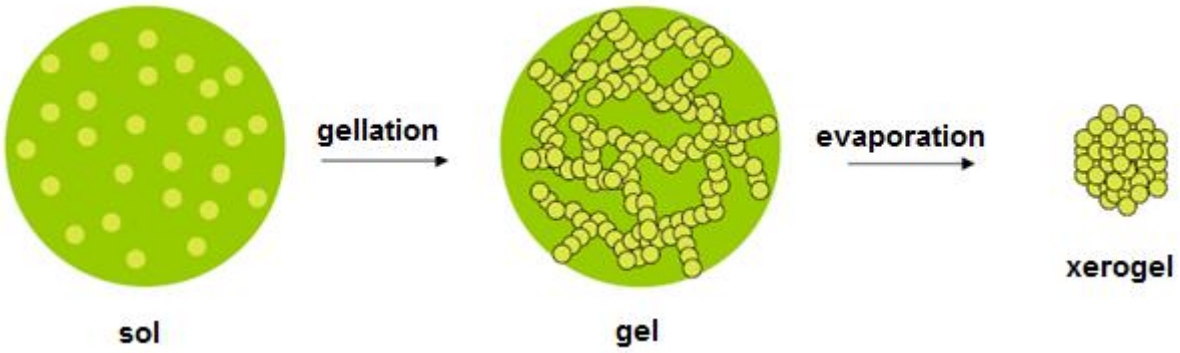

Fig. III.1 *Main stages in xerogels synthes.*

2. Differential thermal analysis

The differential thermal analysis (DTA) and thermogravimetric analysis (TGA) runs were recorded with DTG-60H Shimadzu derivatograph at a heating rate of 10 °C/min from room temperature to 1250 °C. Alumina open crucibles and α-alumina powder as reference material were used, and the measurement was made in flowing atmosphere of nitrogen/air at a flow rate of 70 ml/min.

The DTA curves (Figs III.2 and III.3) point out around 100 °C an intense endothermic peak in DTA curve, associated in TGA curve with a mass loss of 13.5 % due to the removal of physically adsorbed water and alcohol remained in sample after the hydrolysis and polycondensation of the inorganic components in the sol-gel process. The exothermic peak around 352 ^{o}C and the endothermic one at 421 ^{o}C are accompanied in TGA curve by a mass loss of 19.7 % and 17.9 % respetively, mainly due to combustion of residual organic groups and to nitrates decomposition, and respectively to dehydroxylation [29-31].

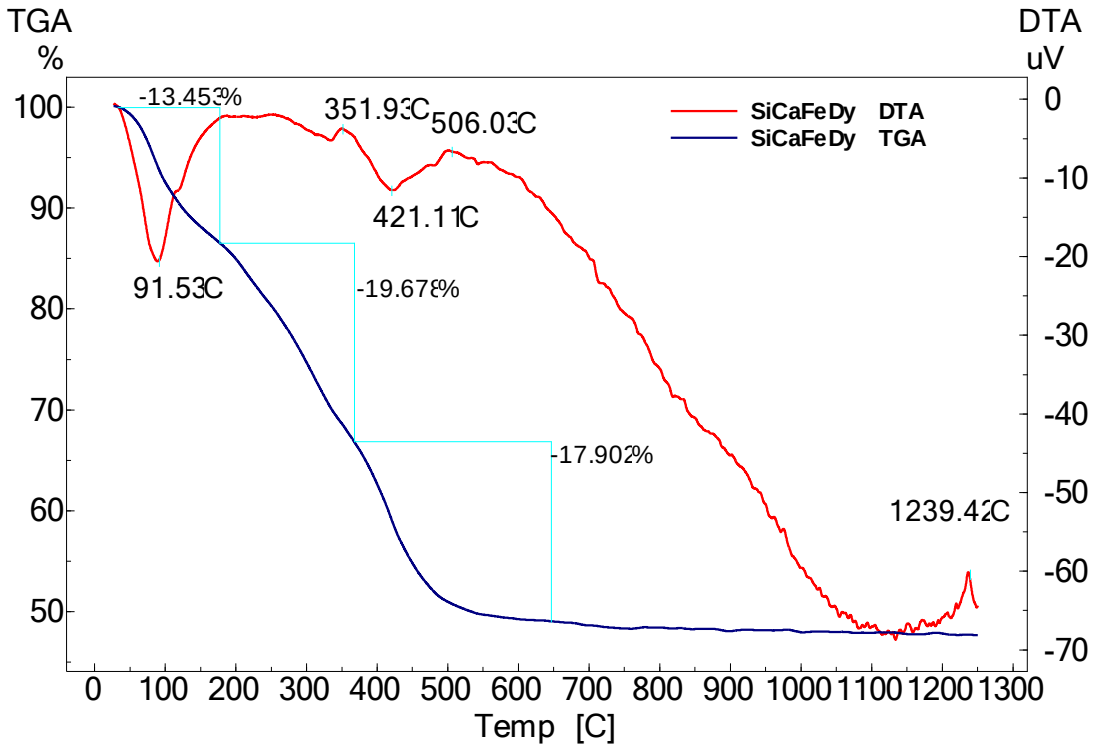

Fig. III.2 *DTA/TG curves of the $50SiO_2 \cdot 30CaO \cdot 10Fe_2O_3 \cdot 10\ Dy_2O_3$ sample dried at 110 ^oC.*

The last event in DTA run is denoted by the 1239 ^oC exothermic peak and points out the development of a crystalline phase. The desired phases for the investigated composition are those involving iron - like magnetite, hematite and zinc ferrite - for potential hyperthermia applications [32], but also wollastonite for bioactivity [33]. For the system with zinc (Fig. III.4) prepared under identical conditions, the endothermic peak at 113 ° C is more intense, and TGA curve corresponds to a weight loss of 27.8%, which shows that the sample held twice plenty of water and alcohol by adding zinc oxide. The exothermic peak around 261 ^oC and the endothermic one at 406 ^oC are accompanied in TGA curve by a mass loss of 11.5 % and 18.4 % respectively, mainly due to combustion of residual organic groups and to nitrates decomposition, and respectively to dehydroxylation. At higher temperatures, it is noted two exothermic events at 800 and about 1200°C, associated with the crystallization transformation.

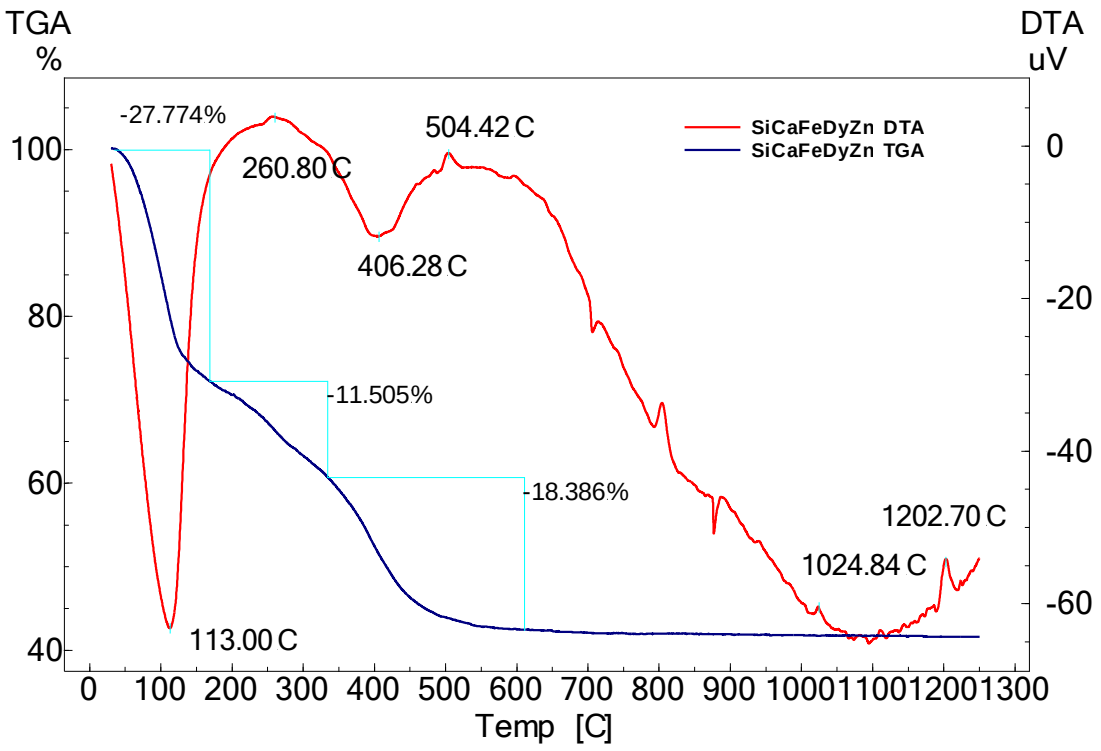

Fig. III.3 *DTA/TG curves of the $50SiO_2 \cdot 28CaO \cdot 10Fe_2O_3 \cdot 10\ Dy_2O_3 \cdot 2ZnO$ sample dried at 110 ^oC.*

Based on DTA/TG results, the thermal treatments were applied for 3 hours at 500, 800 and 1200 °C, in order to remove the residual components and to develop nanostructured magnetic phases with a view to hyperthermia.

Table 1. *BET specific surface area and mean pore volume of thermally treated samples.*

Treatment temperature (^oC)	**Surface area (m^2/g)**		**Pore volume (cm^3/g)**	
	SiCaFeDy	**SiCaFeDyZn**	**SiCaFeDy**	**SiCaFeDyZn**
500	98	80	0.29	0.25
800	52	32	0.17	0.11
1200	< 1	< 1	-	-

The colour of the samples changed function of treatment temperature. After 500 and 800 ^oC treatments, the samples keep a brick-red colour, while after 1200 °C they become

gray. On the other hand, the surface area and mean pore volume for the heat treated samples (Table 1) are diminished with increasing treatment temperature, and after 1200 °C treatment these values fall under the detection limit. The thermal contraction of pore volume, especially in 1200 °C treated sample, is a less advantageous effect, because the porosity is an important property when the application aims the ingrowth of new tissue into the pores.

3. Characterization by X-ray diffraction

X-ray diffraction (XRD) analyses were made on a Shimadzu XRD-6000 diffractometer using Ni-filtered CuK_α radiation ($\lambda = 1.5418$Å) at a scanning speed of 2º/min.

The XRD patterns of $50SiO_2 \cdot 30CaO \cdot 10Fe_2O_3 \cdot 10\ Dy_2O_3$ system (Fig. III. 4) indicate the amorphous state of the 110 ^oC dried sample and the tendency to structural ordering already after 500 ^oC treatment. The structural changes in the still predominant amorphous sample treated 800 ^oC lead to further growth of the crystalline germs of hematite and magnetite evidenced after 500 ^oC treatment and to a broad halo assigned to the prevalent structurally disordered phase.

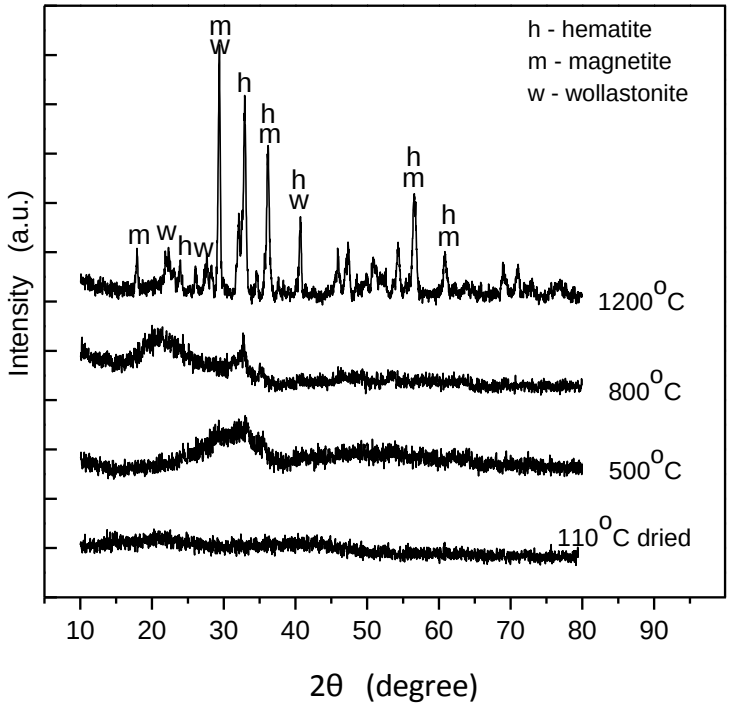

Fig. III. 4*. X-ray diffractograms of $50SiO_2 \cdot 30CaO \cdot 10Fe_2O_3 \cdot 10\ Dy_2O_3$ samples after thermal treatment at different temperatures.*

After 1200 ^{o}C treatment, the XRD pattern shows diffraction lines assigned to hematite (Fe_2O_3), magnetite (Fe_3O_4) and wollastonite ($CaSiO_3$), but the diffraction peaks at 46.1^{o} and 47.4^{o} could suggest the growth of andradite ($Ca_3Fe^{3+}{}_2(SiO_4)_3$) (JCPDS#: 86-0550, 89-3854**,** 76-0186, 10-288). At the same time, beside $CaSiO_3$ crystalline phase possible contributions from Ca_2SiO_4 (JCPDS#: 76-0799) and $CaSi_2O_5$ (JCPDS#: 33-0305) could be added to the diffraction peaks.The size of the crystallites, as determined with Scherrer equation, is below 40 nm for all crystalline phases occurred after heat treatment. The development of nanostructured crystalline phases is expected to enhance their bioactivity [8, 9].

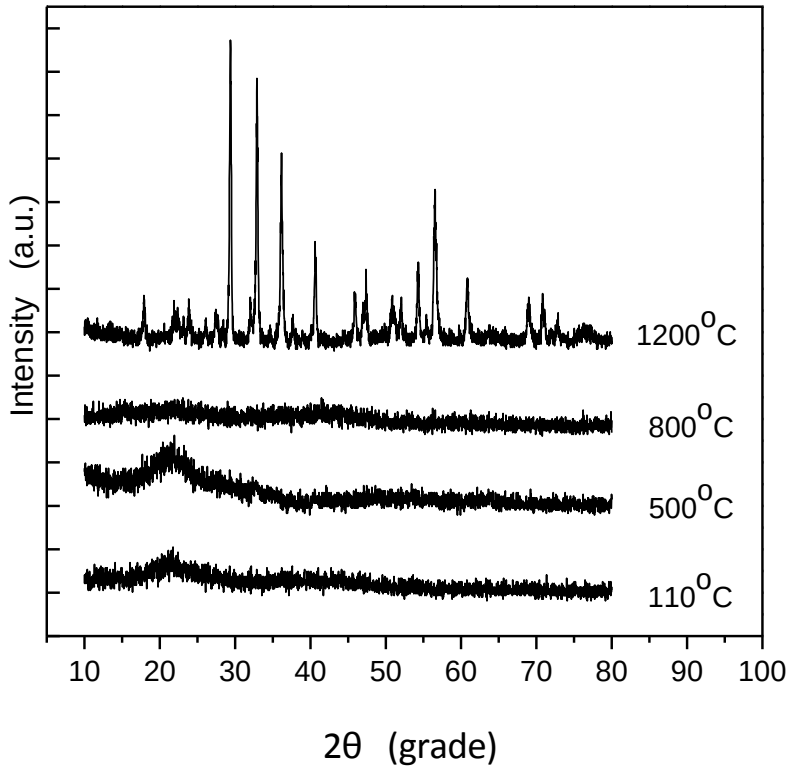

Fig. III.5 *X-ray diffractograms of 50SiO$_2$·28CaO·10Fe$_2$O$_3$·10 Dy$_2$O$_3$·2ZnO samples after thermal treatment at different temperatures.*

The diffraction patterns (Fig. III.5) of zinc containing samples indicate a completely disordered structure even after 800 ^{o}C treatment, denoting that ZnO even in such a low amount, of only 2 mol%, hinders the growth of crystalline phases in this system. Because ZnO may act both as network modifier and as intermediate oxide, for the investigated system it acts as intermediate oxide playing the role of network former which impedes the development of the incipient crystalline phases observed in the system without ZnO. The structural changes are evident after 1200 ^{o}C treatment and very similar with that observed for the system without zinc after the heat treatment carried out under the same conditions.

The size of the crystallites (as determined with Scherrer equation $D = \frac{k\lambda}{\beta \cos\theta}$, where D – crystallite size in Å, k – shape factor, λ – wavelength of X radiation, β - the line broadening at half the maximum intensity (in radians), θ - diffraction angel corresponding to the considered line) is below 40 nm for all crystalline phases occurred after heat treatment in SiCaFeDy system, and slightly higher for SiCaFeDyZn system (Table 2).

The development of nanostructured crystalline phases is expected to enhance their bioactivity [36].

***Table 2**. Crystallites size, D, for 1200 ^{o}C treated samples.*

Diffraction line 2θ	**D (nm)**	
	SiCaFeDy	**SiCaFeDyZn**
29.5	35	35
32.9	27	46
36.2	26	33
40.6	35	37
56.6	19	30

4. Characterization by UV-Vis spectroscopy

UV-visible absorption spectra were recorded at room temperature with a SPECORD 250 Plus spectrophotometer in the wavelength range of 380-800 nm.

The UV-Vis analysis of SiCaFeDy system shows a high similarity for the 110 ^{o}C dried sample and the samples thermaly treated at 500 ^{o}C and 800 ^{o}C. The only clear difference consists in the absorption band occuring at 758 nm in the spectrum recorded from the 110 ^{o}C dried sample (Fig. III.6). This band arises from the water still existing in the dried xerogel. In fact, water does not absorb and is almost perfectly transparent in the near UV or visible range, but it absorbs in the near infrared and shows at room temperature five prominent absorption bands at 760, 970, 1190, 1450 and 1940 nm.

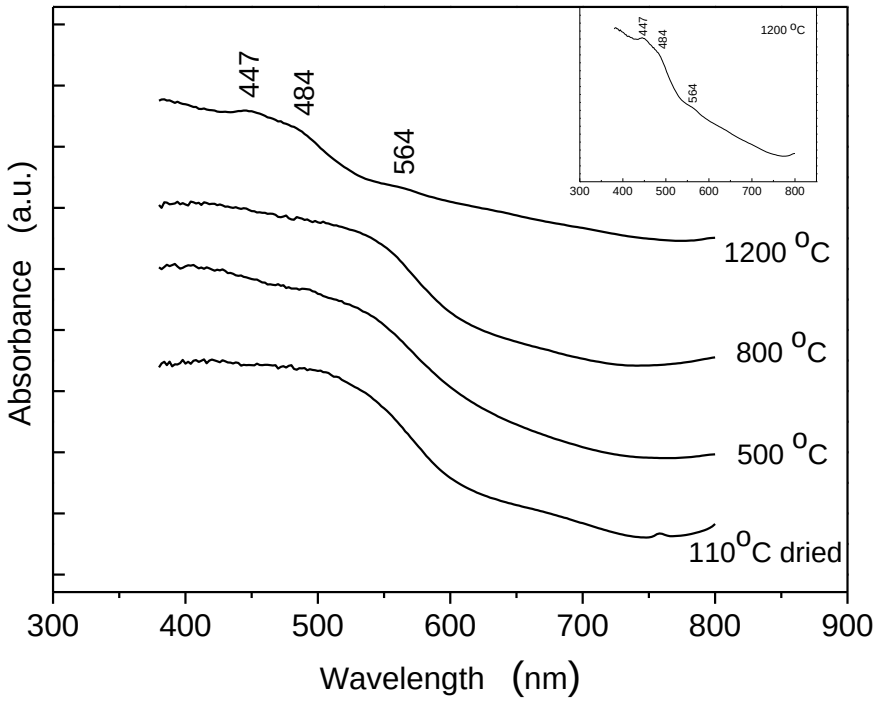

Fig. III.6 *UV-Vis spectra of $50SiO_2 \cdot 30CaO \cdot 10Fe_2O_3 \cdot 10\ Dy_2O_3$ samples after thermal treatment at different temperatures. The absorption features of 1200 °C treated sample can be better observed in inset.*

Interesting changes are evidenced in the spectrum recorded from 1200 °C tretated sample. Three weak absorption bands/shoulders, namely at 447, 484 and 564 nm, occur in the visible range. They are related to the nanocrystalline phases developed in this sample, and provide a consistent structure-property relation. It was recently reported that the absorbance at 440 nm denotes the presence of iron oxide nanoparticles [39].

At the same time, the increase of nanocrystallites size moves the absorption to higher wavelength [40]. Nevertheless, the shift of the electronic absorption bands may occur from the shape modifications of the nanoparticles as well as from their aggregation [41, 42]. Absorption peaks at 552 and 589 nm were reported also for magnetic nanoparticles incorporated in other matrices for biological applications [43].

For zinc containing system SiCaFeDy Zn the UV-Vis spectrum is sensibly different after 1200 °C treatment (Fig. III.7), as compared with SiCaFeDy system, and these changes are easier observed in Fig. III.8.

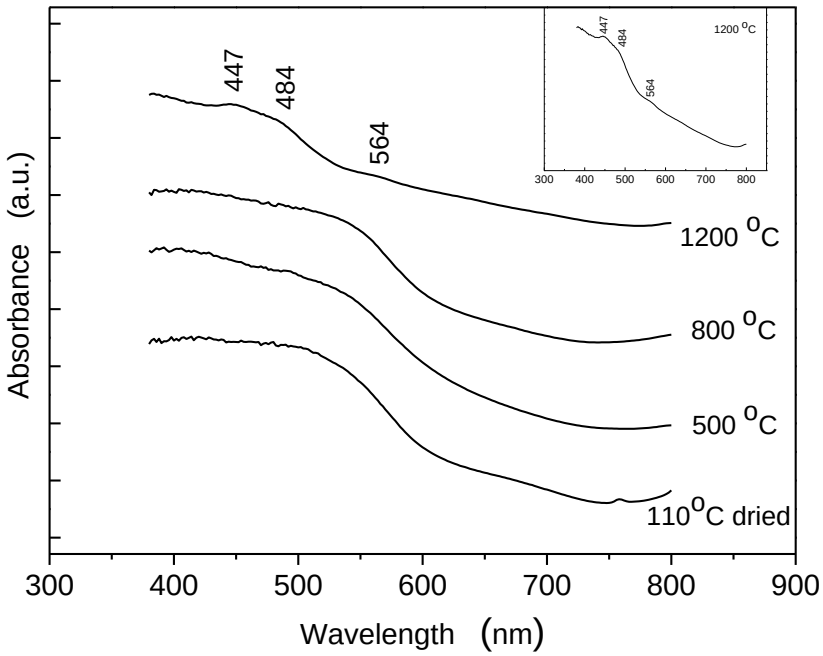

Fig. III.7 *Spectrele UV-Vis spectra of* $50SiO_2 \cdot 28CaO \cdot 10Fe_2O_3 \cdot 10\ Dy_2O_3 \cdot 2ZnO$ *samples treated at different temperatures. For a better observation of the spectral changes occurred after 1200 ° C treatment, this spectrum is shown in enlarged absorbance scale in inset.*

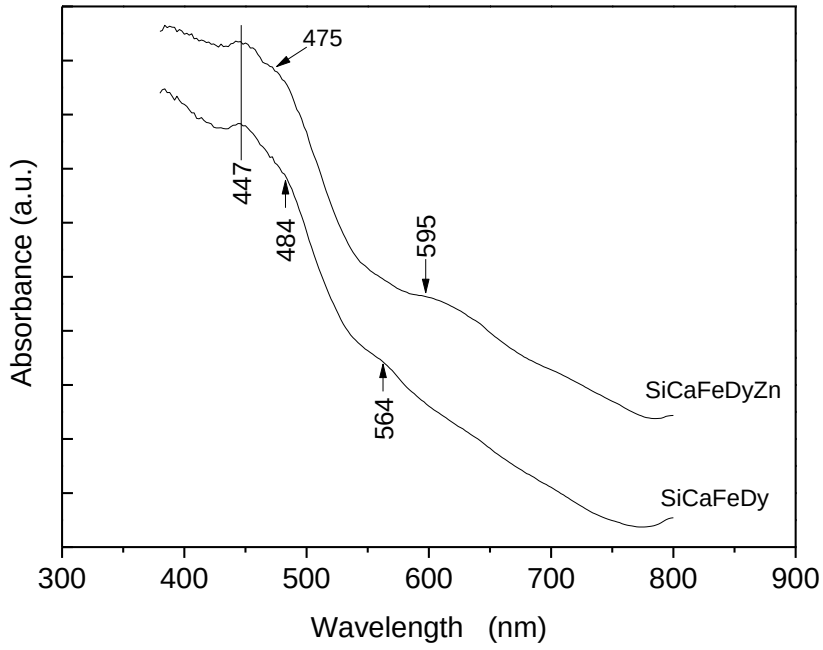

Fig. III.8 *Spectrele UV-Vis spectra of samples without zinc and with 2 mol% ZnO, after 1200* ^{o}C *treatment.*

In both samples a first absorption band occurs around 447 nm, the second absorption band occurs at very slightly shifted wavenumbers, but the third one is clearly shifted to larger

wavenumbers for the zinc containing sample, and the result points out the larger size of the crystallites developed in SiCAFeDyZn than in SiCAFeDy. Actually, X-ray diffraction data showed similar results concerning the crystalles size (Table 2).

5. Characterization by IR spectroscopy

More detailed information on structural changes was obtained by means of FTIR analysis particularly focussed on the network structure. FTIR spectra were recorded in the range of 4000-400 cm^{-1} with a spectral resolution of 2 cm^{-1}, in absorption mode, with a FT/IR-6200 Jasco Spectrometer by using the KBr pellet technique. The pellets were prepared by mixing 2 mg of powdered sample with 200 mg KBr.

The structural ordering upon heat treatment depends on the peculiarities of the elements occurring in the composition of the amorphous oxide compound. The properties regarding coordination number, field strength, Pauling electronegativity and single bond strength with oxygen of the cations entering in the investigated samples are summarized in Table 3. The cationic field strength is expressed by the ratio of the cation charge to the square of the ionic radius.

Table 3*. Coordination number, ionic radius, field strength, Pauling electronegativity and single bond strength for the cations from $50SiO_2{\cdot}30CaO{\cdot}10Fe_2O_3{\cdot}10Dy_2O_3$ and $50SiO_2{\cdot}28CaO{\cdot}10Fe_2O_3{\cdot}10Dy_2O_3{\cdot}2ZnO$ systems.*

Cation	**Coordination number**	**Shannon ionic radius (Å)** [47, 48]	**Cation field strength ($Å^{-2}$)**	**Electronegativity (Pauling units)** [49]	**M–O strength (kJ/mol)** [49]
Si^{4+}	4	0.40	25	1.90	799.6 ± 13.4
	6	0.54	13.72		
Ca^{2+}	6	1.14	1.54	1.00	402.1 ±16.7
	8	1.26	1.26		
Dy^{3+}	6	1.05	2.72	1.22	607 ± 17
	8	1.17	2.19		
Fe^{3+}	4	0.63	7.56	1.83	390.4 ± 17.2
	6	0.78	4.93		
	8	0.92	3.54		
Zn^{2+}	4	0.74	3.65	1.65	159 ± 4
	6	0.88	2.58		
	8	1.04	1.85		

The cations belonging to the conventional glass former oxides are characterized by high field strengths as compared to the cations entering as modifiers. In this approach, in the investigated system CaO, Dy_2O_3 and Fe_2O_3 are expected to play the role of modifier oxides in the silicate glass network built up from tetrahedral [SiO_4] structural units. On the other hand, the higher the ionic field strength, the greater the stability of glass toward crystallization [45]. For nonmetallic glasses, it was also reported that the thermal stability against crystallization decreases with the electronegativity difference [46]. Considering the lowest field strength and electronegativity of calcium ions versus that of dysprosium and iron ions, it is expected to prevail the development of calcium silicate crystalline phases in the silicate vitreous network.

At wavenumbers between 4000 cm^{-1} and 2000 cm^{-1} only few differences are evidenced in FTIR spectra (Fig. III.9a). The signal at 2358-2343 cm^{-1} is not related to samples; it comes from registration and can be used even as a reference.

The broad band located between 3350-3600 cm^{-1} is assigned to O-H erences due to increasing treatment temperature (Fig. III.9b). The absorption band around 1640 cm^{-1} is commonly assigned to O-H bending vibration [51], but can occur also from vibrations of the SiO_2 network and is often hidden by water O-H band [40]. In our spectra one remarkes that the band intensity does not decrease even after 1200 ^oC treatment, and is steady slightly shifted to lower wavenumbers with increasing treatment temperature (1647, 1637 and 1631 cm^{-1}, for samples treated at 500, 800 and 1200 ^oC, respectively) that makes unlikely its assignment only to water molecules.

The FTIR spectra reveal an absorption band at 1465 cm^{-1} due to C-H bending for methyl and methylene group and a characteristic very narrow band for nitrates at 1385 cm^{-1} [52, 53] only in the 500° C treated sample, and disappear after thermal treatment at higher temperatures. The spectra are dominated by a broad signal in the 750-1300 cm^{-1} spectral range, where the stretching vibrations of the Si-O-Si and Si-O-M (M = Ca, Fe) bridges occur [54, 55]. In 750-1300 cm^{-1} spectral range are recorded Si-O-Si bending vibrations around 800 cm^{-1}, and at higher wavenumbers Si-O-Si asymmetric stretching vibration; Si-O-Si bending vibrations give absorption bands also in the range of 500 - 400 cm^{-1} [56, 57].

A comparison between the FTIR spectra of the samples treated at different temperatures and the infrared absorption bands recorded from γ-Ca_2SiO_4 (496, 520, 565, 819, 859, 953 cm^{-1}) and β-$CaSiO_3$ (452, 471, 508, 566, 642, 680, 904, 925, 964, 1019, 1056, 1087 cm^{-1}) [80] crystalline phases sugessts, by the occurence of 520 cm^{-1} band, the growth of γ-Ca_2SiO_4 after 800 ^oC treatment.

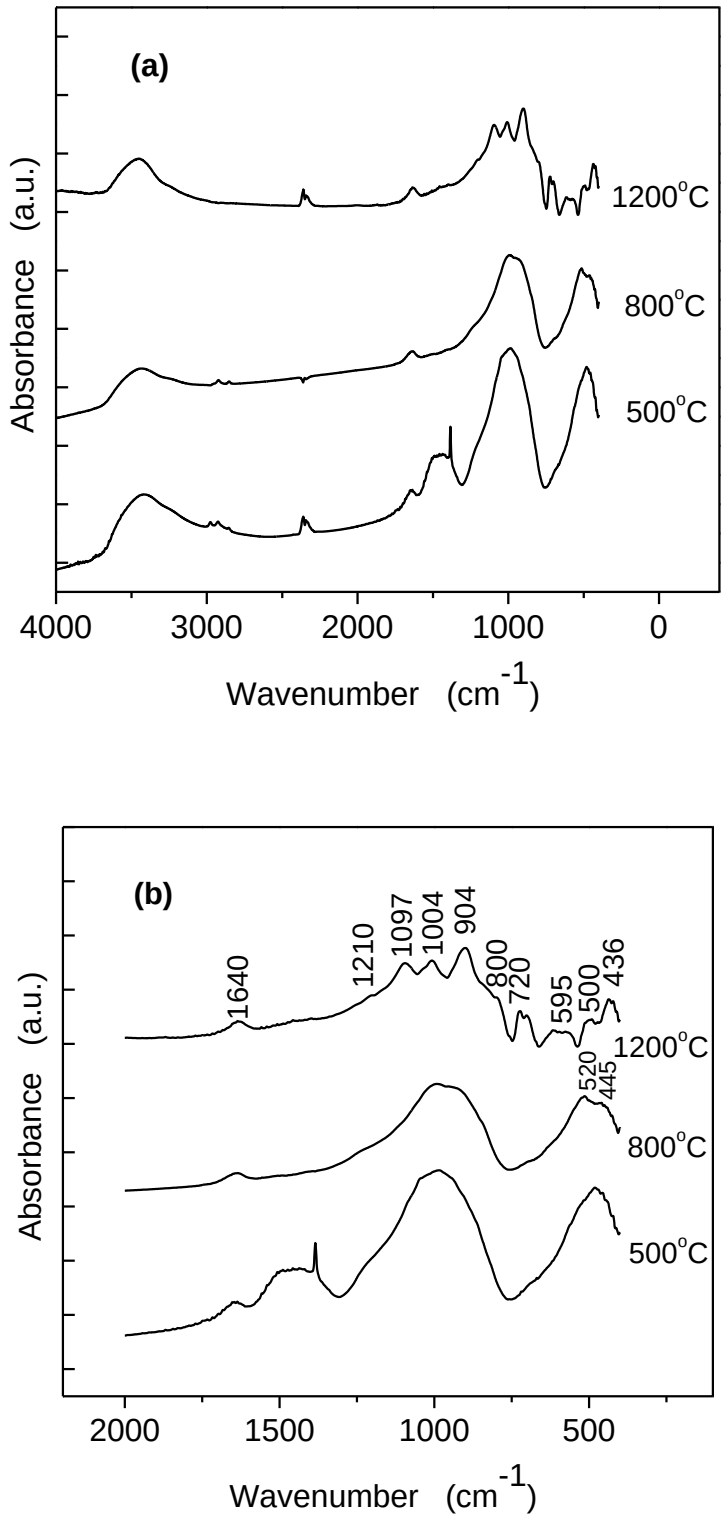

Fig. III.9 *FTIR spectra of $50SiO_2 \cdot 30CaO \cdot 10Fe_2O_3 \cdot 10Dy_2O_3$ system treated at different temperatures, shown in whole registration range (a), and expanded in 400-2000 cm^{-1} region (b).*

In the infrared spectrum of the 1200 ^{o}C treated samples only the band at 500 cm^{-1} could be further related to some extent to γ-Ca_2SiO_4 phase, but egually to β-$CaSiO_3$, while the bands at 640, 682 and 904 cm^{-1} strongly prove the development of β-$CaSiO_3$ phase.

The spectra deconvolution in 750-1300 cm^{-1} range (Fig. III.10) shows a good agreement between simulated and experimental spectra using four component bands. For the 500 ^{o}C heated sample the large band is composed by the superposition of three components at 1210, 1004 and 877 cm^{-1}. The dominant component occurs close to 1004 cm^{-1} and is characteristic for amorphous silica [58]. The components at 1210 cm^{-1} [59] and 877 cm^{-1} [55] are assigned to Si-O-Si asymmetric stretching vibrations.

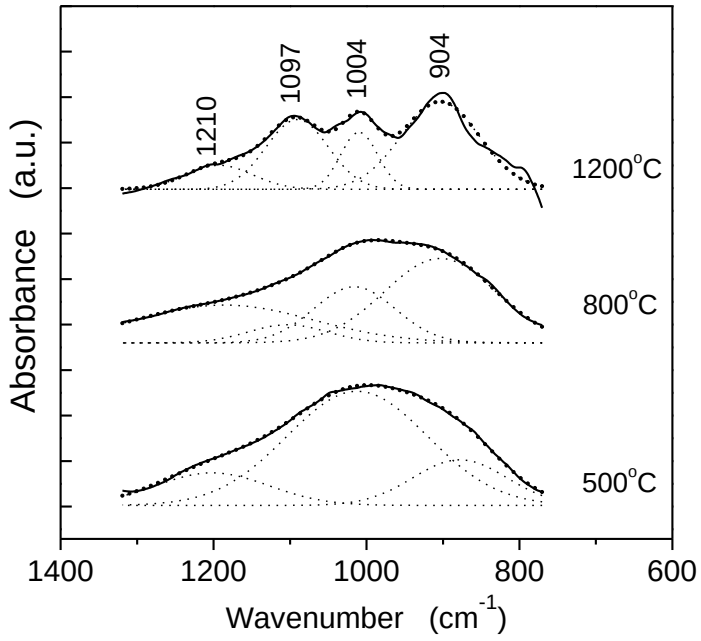

Fig. III.10 *Deconvolution of large absorption band recorded in 750-1300 cm^{-1} spectral range from SiCaFeDy sample after treatments at different temperatures.*

The increase of treatment temperature leads to changes in the contributions of these components and to the forth component at 1097 cm^{-1} (Table 4). At the same time, one remarks that 1004 cm^{-1} component assigned to vitreous silica pronouncedly diminishes while that at 904 cm^{-1} pronouncedly increases. Moreover, after 800 ^{o}C treatment the large absorption band recorded at low wavenumbers, between 400-580 cm^{-1}, contains at 445 and 520 cm^{-1} features (Fig. III. 9) that could include contributions from hematite (Fe_2O_3) [61]. After 1200 ^{o}C treatment well separated absorption bands occur at 1097, 1004, 904, 720, 500 and 436 cm^{-1} due to development of β-wollastonite ($CaSiO_3$) and pseudowollastonite [33, 62, 63]. For the 1200 ^{o}C treated sample one observes around 595 cm^{-1} an absorption band

apparently consisting of two components assigned to stretching vibrations of Fe-O bonds [64], typical for Fe-O vibration in magnetite (Fe_3O_4) [65].

Table 4 *Treatment temperature dependence of different components for SiCaFeDy system, in 750-1300 cm^{-1} spectral range.*

Components wavenumber →	1012 cm^{-1}	1097 cm^{-1}	1004 cm^{-1}	904 cm^{-1}
Treatment temperature ↓	Components contribution (%)			
500 ^oC	15.3	-	66.8	17.9 (877 cm^{-1})
800 ^oC	30.4	6.4	20.7	42.5
1200 ^oC	10.9	29.5	14.3	45.3

The careful inspection of this band points out several contributions (Fig. III.11) at different wavenumbers, denoting that the Fe-O bonds in nanocrystallized magnetite are affected by different vicinities. Actually, the data presented in Table 4 show the consistent diminution of the amorphous phase related to 1004 cm^{-1} component along with the increase of the components assigned to wollastonite. The ratio of amorphous components after 500 and 800 ^oC treatments is 66.8/20.7=3.2 and after 1200 ^oC treatment this ratio becomes 66.8/14.3=4.7.

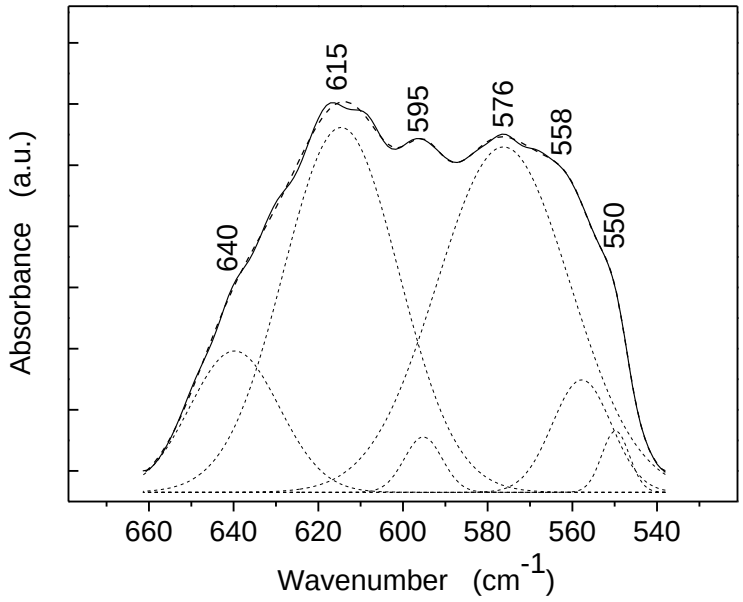

Fig. III.11 *Infrared absorption band centered around 595 cm^{-1}, for SiCaFeDy sample after 1200 ^oC treatment.*

The components at 550 and 558 cm^{-1} are assigned to hematite, the prevalent component at 577 cm^{-1} to magnetite, 595 cm^{-1} is typical for Fe-O vibration in magnetite (Fe_3O_4); an absorption band at 611 cm^{-1} was assigned to Fe-O bending vibrations of the magnetite nanoparticles [80]. The component at 640 cm^{-1} occurs from β-$CaSiO_3$ crystalline phase, as presented above.

Dysprosium presence in the system should also be taken into account. Typical Dy-O vibrations occur at 550 or 555 cm^{-1} with a broad shoulder at 580 cm^{-1}, and vibrations of Si-O-Dy bonds could occur at 1017 cm^{-1} [66]. The broad shoulder at 580 cm^{-1} could contribute beside magnetite to the the prevalent component at 577 cm^{-1}. It was reported that large radius ions occuring in the vecinity of magnetically ordered iron oxide phases lead to a shift the Fe-O infrared absorption bands to higher wavenumbers [67]. For our system, beside the presence of calcium and dysprosium large radius ions, to this effect could also contribute the difference in the bond strengths of Dy-O and Fe-O, namely Dy-O strength is much higher than that of Fe-O (Table 3).

FTIR analysis results for zinc samples shows a number of similarities with the results presented for the system that was not replacing 2 mol% CaO with ZnO. Recorded spectra are presented in Fig. III.12. The thermal treatment effects are emphasized more strongly in the 1300-400 cm-1 (Fig. III.12b).

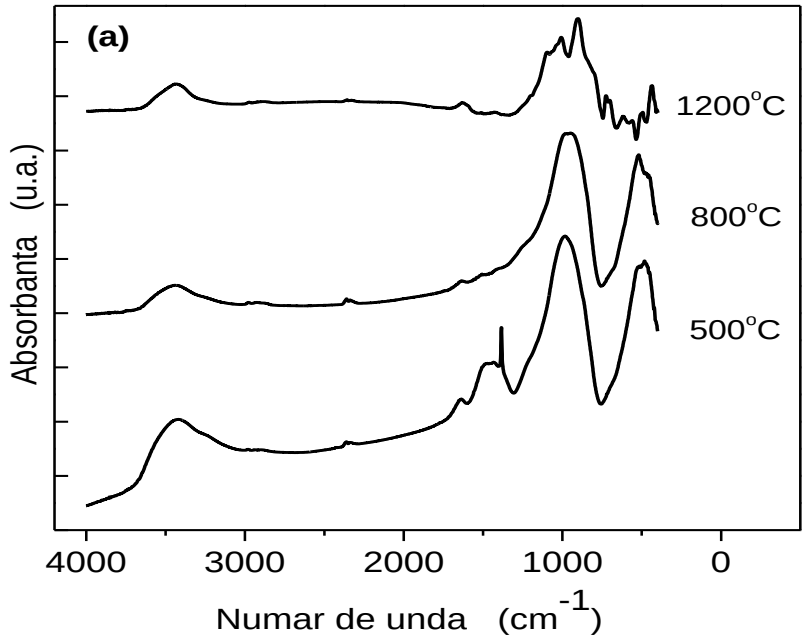

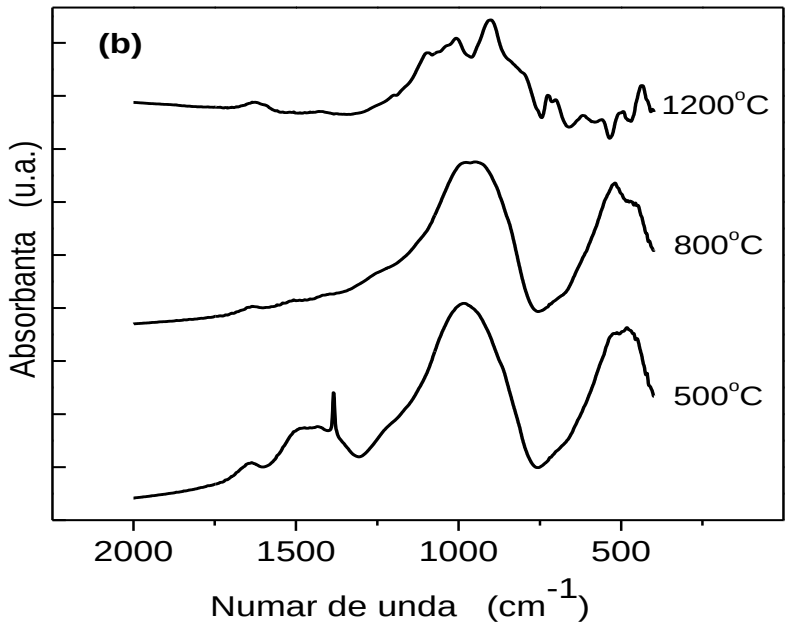

FigIII.12 *FTIR spectra 50SiO_2 system 28CaO 10Fe_2O_3 0Dy_2O_3 2ZnO treated at different temperatures, the entire recording (a) and the region 400-2000 cm-1 (b)*

The compositional change in the two systems are very minor, it is expected that it will not cause structural effects. Comparative, the analysis of the absorption bands in the 400 - 2000 cm^{-1} spectral range is indicating no notable differences after the thermal treatment at 500 to 800 ° C (Fig. III.13 and III.14) but highlights the differences due to the introduction of zinc oxide when the samples were treated at 1200 °C (Fig. III.15).

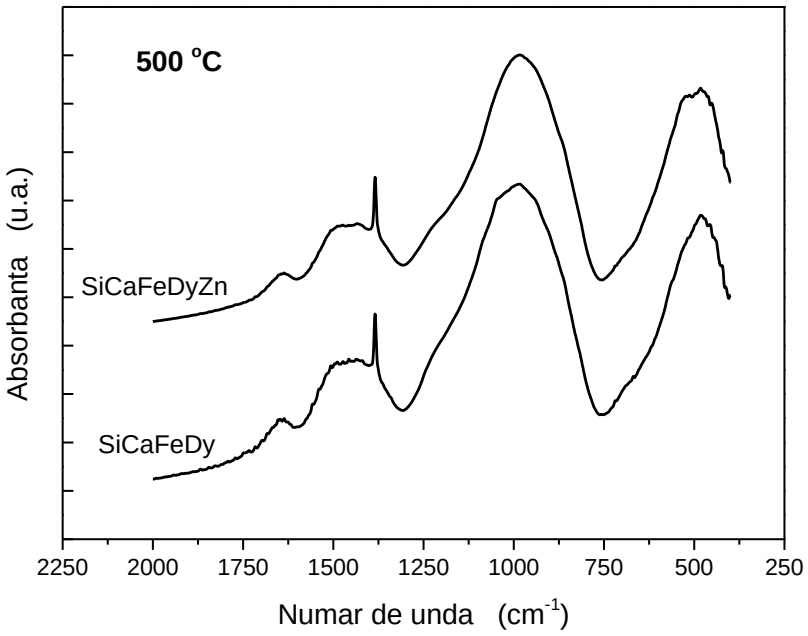

Fig. III.13 *FTIR spectra for the two systems treated at 500 °C.*

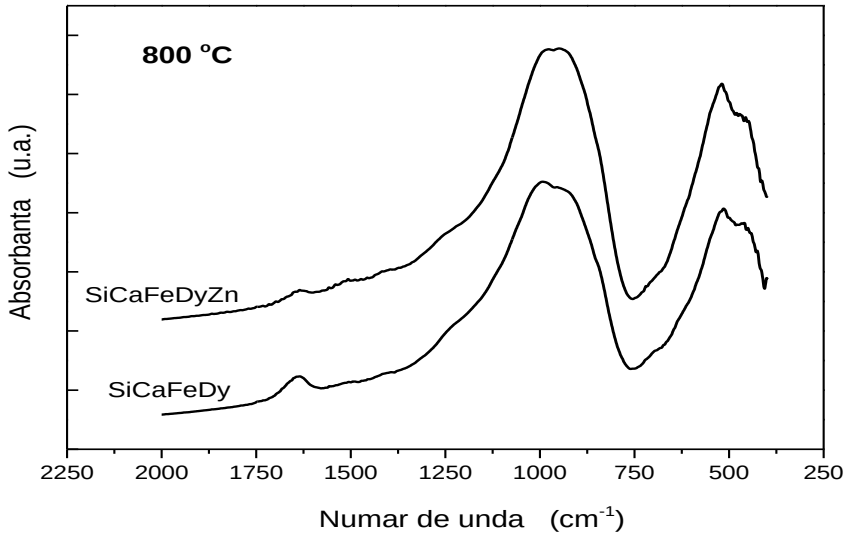

Fig. III.14 *FTIR spectra for the two systems treated at 800 °C.*

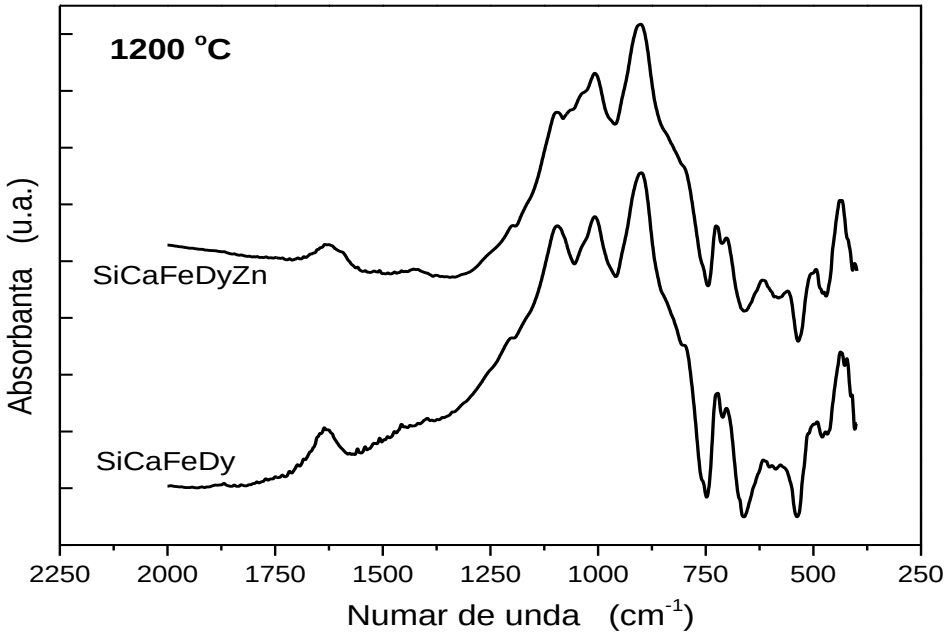

Fig. III.15 *FTIR spectra for the two systems treated at 1200 °C.*

The analysis of the two systems, in the 1340 – 750 cm^{-1} spectral range (Fig. III.16) and of the infrared absorption band around 595 cm^{-1} (Fig. III.17) show a higher number of components in the zinc containing system due to ZnO influence on both wollastonite (Fig. III.16) and iron oxide crystallites (Fig. III.17).

By comparing the 1097 cm^{-1} and 1004 cm^{-1} absoption bands assigned to wollastonite and to vitreous phase, respectively, one remarks that the vecinity of wollastonite crystallites is

influenced by the small ZnO amount added to SiCaFeDy system (Fig. III.16) denoted by the vibrations of Si-O-Si bond, but it does not affect the Si-O-Ca bonds containing nonbridging oxygen atoms [60].

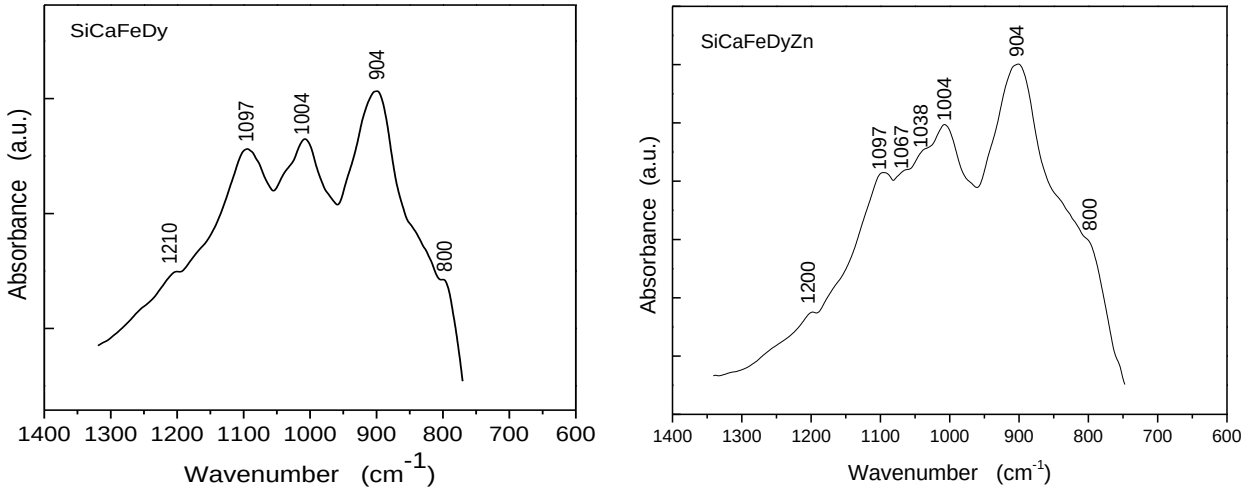

Fig. III.16 *FTIR spectra of 1200 ^{o}C treated samples displayed in 1340 – 750 cm^{-1} spectral region.*

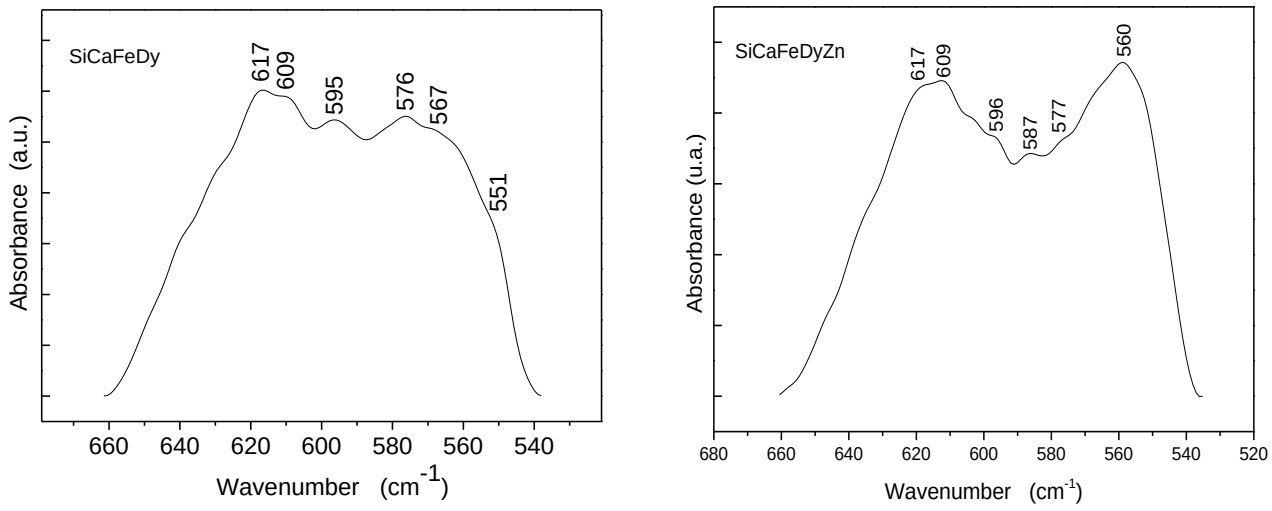

Fig. III.17 *FTIR band around 595 cm^{-1} recorded from 1200 ^{o}C treated samples.*

These differences are related to the 2 mol% replacement of CaO by ZnO, and while CaO acts as a strong network modifier the ZnO enters as an intermediate oxide.

6. Characterization by EPR spectroscopy

The main lines from the EPR spectra of 500 and 800 ^{o}C treated samples are characterized by g = 4.24 and g = 2.02 resonance lines (Fig. III.18). The first line is assigned to isolated Fe^{3+} ions disposed in sites of low symmetry characterized by high crystal fields, and that at g = 2.02 is assigned to Fe^{3+} ions disposed in sites of octahedral symmetry, with low crystal fields, or associated in clustes [68, 69]. A third EPR signal at g = 7.66 is also recorded from the 500 ^{o}C treated sample and is assigned to Fe^{3+} ions disposed in sites of axyal symmetry [73].

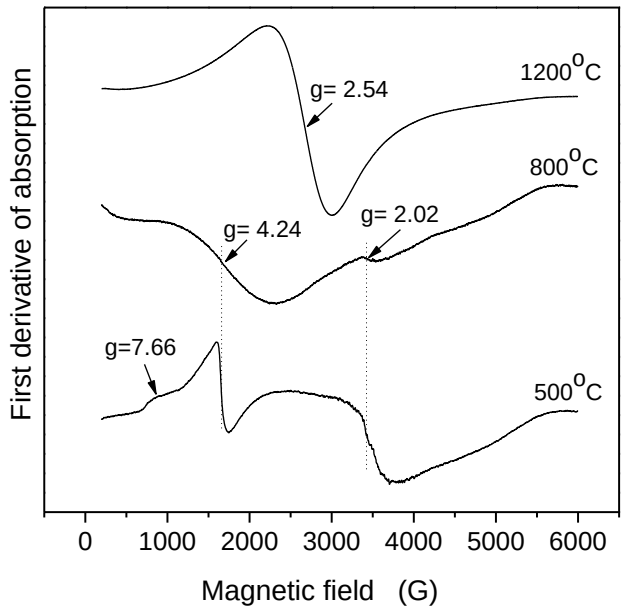

Fig. III.18 *Fe^{3+} EPR spectra of $50SiO_2 \cdot 30CaO \cdot 10Fe_2O_3 \cdot 10Dy_2O_3$ system after treated at different temperatures.*

The EPR spectrum recorded from the 1200 ^{o}C treated sample consists of a single large resonance line at g = 2.54 given by Fe^{3+} ions disposed in randomly oriented iron oxides magnetite-maghemite nanoparticles [74]. Fe^{2+} ions species are also present along with Fe^{3+} ions but they are EPR silent at room temperature. The ferromagnetic magnetite (Fe_3O_4) and ferrimagnetic maghemite (γ-Fe_2O_3) are by far the most commonly employed magnetic materials for biomedical applications and both are of interest also for hyperthemia in cancer therapy [75].

For 500 ^{o}C treated SiCaFeDyZn sample the Fe^{3+} EPR spectrum (Fig. III.19) does not differ from that obtained for SiCaFeDy sample after 500 ^{o}C treatment (Fig. III.18); it consists of the same three resonance lines occurring at g = 2.02, 4.24 and 7.66 (Fig. III.19).

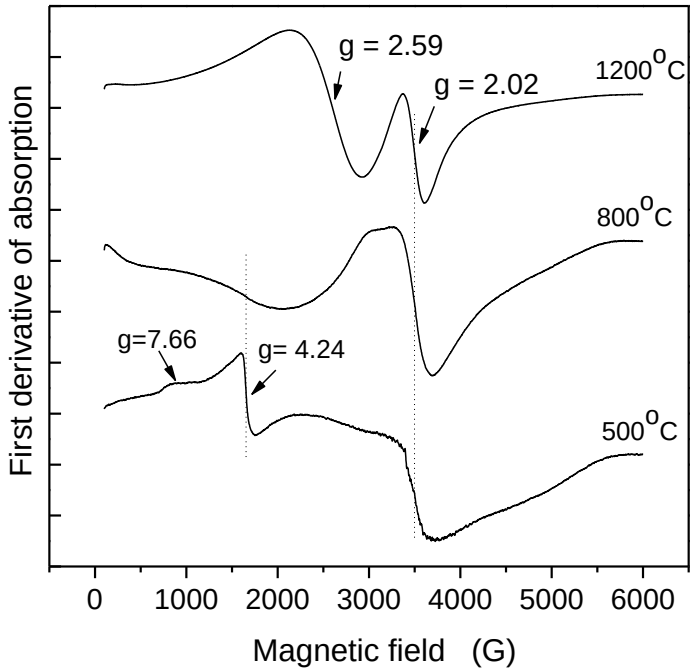

Fig. III.19 *Fe^{3+} EPR spectra of $50SiO_2 \cdot 28CaO \cdot 10Fe_2O_3$ $10Dy_2O_3 \cdot 2ZnO$ system after treated at different temperatures.*

The Fe^{3+} EPR spectra differ for the 800 si 1200 ^oC treated samples. The g = 2.02 resonance line is prevalent in the EPR spectrum of SiCaFeDyZn sample treated at 800 ^oC, and this line is recorded even after 1200 ^oC treatment, in contrast to SiCaFeDy sample wherin Fe^{3+} ions are not more evidenced in sites of octahedral symmetry with low crystal field, or as Fe^{3+} ions aggregated in clusters. The width of the resonanve line at g = 2.59 in SiCaFeDyZn sample is 795 G, very close to the width of g = 2.54 line recorded from SiCaFeDy sample. This result supports the growth of nanostructured magnetite/maghemite crystalline phase.

Magnetite and maghemite have the same structure and cannot be decelated by usual X-ray diffraction analysis [76]. The electron paramagnetic resonance is a very strong tool for the investigation of paramagnetic ions like Fe^{3+} in diluted systems [77] but is less applied for systems containing phases with residual magnetization because in such cases strong dipole-dipole interactions or magnetic coupling occur that lead at room temperature to very intense and large signals which cannot be univocally assigned to a certain magnetic phase [77-79]. The large resonance line at g = 2.59 is assigned to Fe^{3+} ions in magnetite/maghemite [74, 79, 80].

Magnetization curves (Fig. III.20) recorded at room temperature, at the laboratory of the Institute of Physics' Ioan Ursu, have a very narrow hysteresis loop, which sustain a

superparamagnetic behavior of investigated systems. For the SiCaFeDy system, respectively for the SiCaFeDyZn system, the residual magnetization is about 0.6 to 0.4 emu/g and the coercive field of approximately 25 to 35 G (1G = 10^{-4} T), which are consistent with the literature [81].

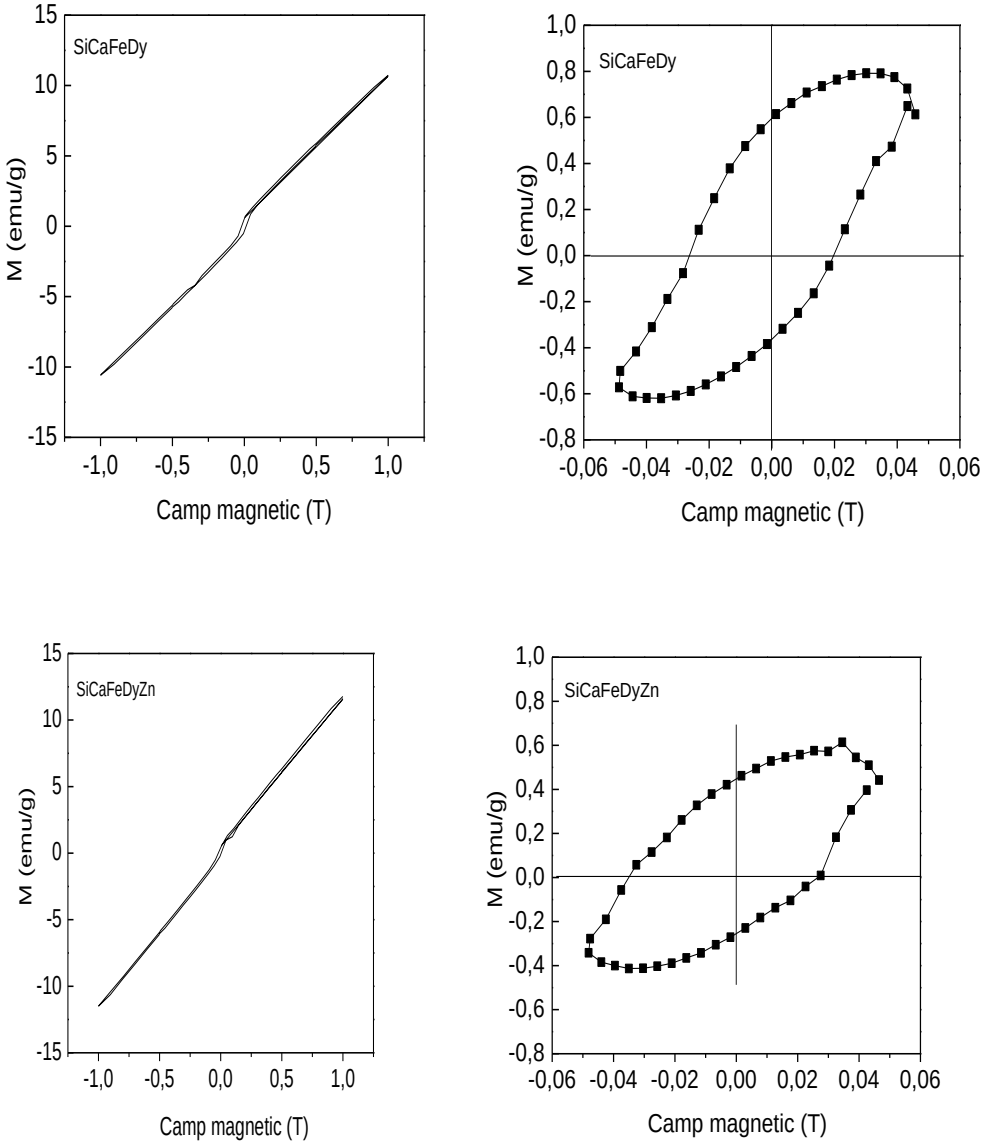

Fig. III.20 M*agnetization curves for $50SiO_2 \cdot 30CaO \cdot 10Fe_2O_3 \cdot 10Dy_2O_3$ and $50SiO_2 \cdot 28CaO \cdot 10Fe_2O_3\ 10Dy_2O_3 \cdot 2ZnO$ samples, treated at 1200^oC*

A very recently published paper [11] reports on iron oxide containing yttrium aluminosilicate microparticles tested intratumorally in an animal model of liver cancer for localized therapeutic hyperthermia. Based on yttrium activation, the hyperthermia can be combined with brachytherapy for a more efficient thermoradiotherapy.

Conclusions

- Calcium-silicate systems with iron and dysprosium $50SiO_2 \cdot 30CaO \cdot 10Fe_2O_3 \cdot 10\ Dy_2O_3$ and $50SiO_2 \cdot 28CaO \cdot 10Fe_2O_3 \cdot 10$ Dy2O3·2ZnO, wherin calcium oxide ws partially replaced by zinc oxide, were obtained by sol-gel method. The development of wollastonite and magnetite/maghemite nanoccrystalline phases was followed in these systems, for possible biomedical applications.
- SiO_2 were CaO introduced as glass network former and modifier, respectively, because they impart bioactivity to calco-silicate glasses. Fe_2O_3 acts as network modifier and was introduced to form magnetic nanocrystalline phases considered for medical applications by hyperthermia therapy. The addition of Dy_2O_3 had in view the possibility to activate the stable isotope ^{164}Dy, by irradiation with thermal neutrons, to the radioactive isotope ^{165}Dy, because ^{165}Dy is a beta-emitter with proper half-life (2.3 hr) for *in situ* radiotherapy. Zinc accelerates the bone healing processes, reduces the bone resorption and if introduced in bioglasses or a bioceramics it contributes to the improvement of their osteoinductive properties. When ZnFe2O4 crystalline phase is formed, it can contribute as zinc ferrite for hyperthermia.
- According to DTA/DTG results the samples were treated at 500, 800 and 1200 ^oC, for 3 hours, in order to develop wollastonite and magnetite/maghemite nanoccrystalline phases.
- The increasing treatment temperature and the addition of ZnO reduces the specific area and pore volume.
- X-ray diffraction results point out for both systems the development of wollastonite and magnetite/maghemite nanoccrystalline phases with crystallites size below or close to 40 nm, and ZnO addition slightly increases the crystallites size.
- ZnO acts as intermediate oxide and therefore the development of nanoccrystalline phases was achieved in $50SiO_2 \cdot 28CaO \cdot 10Fe_2O_3 \cdot 10$ Dy2O3·2ZnOsystem only after 1200 ^oC treatment.
- UV-Vis analysis pointed out changes in the optical behaviour of 1200 ^oC treated samples. For zinc free system weak absorption bands/sholders were recorded at 447, 484 and 564 nm arising from the nanocrystalline phases, which prove the close relationship between structure and absorption behaviour in the visible spectral range.

- UV-Vis analysis carried out on zinc containing shows that 564 nm absorption is shifted to 595 nm that denotes higher size for the crystallites developed as ZnO replaced 2 mol % of CaO.
- FTIR studies indicate with increasing treatment temperature a pronounced decrease of 1004 cm^{-1} component assigned to vitreous silica, while the 904 cm^{-1} component, assigned to Si-O-Ca vibrations in wollastonite, is amplified; at the same time in the range of low wavenumbers are evidenced infrared absorption bands due to Fe-O bond vibration in magnetic nanostructures.
- The content of 2 mol% ZnO influences the development of nonostructured wollastonite and iron oxides.
- EPR results of 500 ^oC treated samples show the in both systems Fe^{3+} ions are (i) izolated in sites of low symmetry characterisic for intense crystal fields, (ii) in sites of octahedral symmetry, with low crystal field, (iii) in sites of axiall symmetry.
- After 800 ^oC treatment in both systems Fe^{3+} ions occur only (i) izolated in sites of low symmetry characterisic for intense crystal fields, and (ii) in sites of octahedral symmetry, with low crystal field.
- After 1200 ^oC treatment, in $50SiO_2 \cdot 30CaO \cdot 10Fe_2O_3 \cdot 10\ Dy_2O_3$ system all Fe^{3+} ions are disposed in nanostructured magnetite/maghemite, while in$50SiO_2 \cdot 28CaO \cdot 10Fe_2O_3 \cdot 10$ Dy2O3·2ZnO system part of Fe^{3+} ions are still disposed in octahedral symmetry sites, with low crystal field.
- All these resultsshow that the investigated systems may be considered for potential applications in thermoradiotherapy.

References

1. G. Wei, P.X. Ma, Nanostructured Biomaterials for Regeneration, Adv. Funct. Mater. 2008; 18(22): 3566–3582
2. L.L. Hench, H.A. Paschall, Direct chemical bond of bioactive glass ceramic materials to bone and muscle, Journal of Biomedical Materials Research, 1973, 7 (3), pp. 25-42.
3. E. Verne, O. Bretcanu, C. Balagna, C.L. Bianchi, M. Cannas, S. Gatti, C. Vitale-Brovarone, Early stage reactivity and in vitro behavior of silica-based bioactive glasses and glass-ceramics, J Mater Sci: Mater Med (2009) 20:75–87.
4. G. Jell, M. M. Stevens, Gene activation by bioactive glasses, J Mater Sci: Mater Med (2006) 17:997–1002
5. E.M. Erbe, D.E. Day, Chemical durability of Y_2O_3-Al_2O_3-SiO_2 glasses for the in vivo delivery of beta radiation, Journal of Biomedical Materials Research, (1993) 27 (10), pp. 1301-1308
6. D. Arcos, R.P. del Real, M. Vallet-Regi, A novel bioactive and magnetic biphasic material , Biomaterials 23 (2002) 2151-2158.
7. Eniu, D., Cacaina, D., Coldea, M., Valeanu, M., & Simon, S. (2005). Structural and magnetic properties of CaO-P_2O_5-SiO_2-Fe_2O_3 glass-ceramics for hyperthermia. *Journal of magnetism and magnetic materials*, *293*(1), 310-313.
8. Vanea, E., Tămăşan, M., Albon, C., & Simon, V. (2011). Synthesis and characterisation of a new composite aluminosilicate bioceramic. *Journal of Non-Crystalline Solids*, *357*(22), 3791-3796
9. P. Wust, B. Hildebrandt, G. Sreenivasa, B. Rau, J. Gellermann, H. Riess, R. Felix, P.M. Schlag, Hyperthermia in combined treatment of cancer, Lancet Oncol. **3**, 487 (2002).
10. V. Simon, D. Eniu, A. Takacs, K. Magyari, M. Neumann, S. Simon, Iron doping effect on the electronic structure in yttrium aluminosilicate glasses, Journal of Non-Crystalline Solids 351 (2005) 2365–2372.
11. A.C. Gordon, R.J. Lewandowski, R. Salem, D.E. Day, R.A. Omary, A.C. Larson, Localized Hyperthermia with iron oxide-doped yttrium microparticles: steps toward image-guided thermoradiotherapy in liver cancer, Journal of Vascular and Interventional Radiology, 2014, Volume 25, Issue 3, Pages 397–404

12. J.C. Brinker**,** G.W. Scherer, Sol-Gel Science: The Physics and Chemistry of Sol- Gel Processing. San Diego, Academic Press**,** 1990
13. R. Veres, A. Vulpoi, K. Magyari, C. Ciuce, V. Simon, Synthesis, characterisation and *in vitro* testing of macroporous zinc containing scaffolds obtained by sol-gel and sacrificial template method, Journal of Non-Crystalline Solids, 373–374, 57–64 (2013)
14. R. Langer, J. Vacanti, Tissue engineering, Science 260 (1993) 920-926.
15. R. Ciceo-Lucăcel, Măsurători termice, În: Metode experimentale avansate pentru studiul ş i analiza bio-nano-sistemelor, M. Aluas, S. Simon (editori)Casa Cărţ ii de Ş tiinţ ă, Cluj-Napoca, 2012.
16. V. Simon, Metode de investigare a structurii / C. Popa, V. Cândea, V. Simon, D. Lucaciu, O. Rotaru, Ştiința biomaterialelor**.** Biomateriale metalice, Cluj-Napoca, U.T.Press, 2008
17. Andrei Florin Dăneţ , Aanaliză instrumentală, Partea I, Editura Universităţ ii Bucureş ti, 2010.
18. N. Leopold, Spectroscopia de absorbţ ie în infraroş u, În: Metode experimentale avansate pentru studiul ş i analiza bio-nano-sistemelor, M. Aluas, S. Simon (editori)Casa Cărţ ii de Ş tiinţ ă, Cluj-Napoca, 2012.
19. I. Ursu, *Rezonanţ a electronică de spin*. Editura Academiei, Bucureş ti,1965
20. O. Peitl, E.D. Zanotto, F.C. Serbena, L.L. Hench, Compositional and microstructural design of highly bioactive P 2O 5-Na 2O-CaO-SiO 2 glass-ceramics, Acta Biomater. 2012 8 (1), pp. 321-332
21. J.E. White, D.E. Day, Rare earth aluminosilicate glasses for in vivo radiation delivery, Key Engineering Materials, 94-95, 181 (1994)
22. B.L. Vallee, D.S. Auld, Zinc metallochemistry in biochemistry, EXS. 1995; 73:259-77.
23. D.S. Auld, The ins and outs of biological zinc sites, Biometals, 2009, 22 (1) 141-8.
24. M. Ikeuchi, A. Ito, Y. Dohi , H. Ohgushi H. Shimaoka, K. Yonernasu, T. Tatcishi, Osteogenic differentiation of cultured rat and human bone marrow cells on the surface of zinc-releasing calcium phosphate ceramics, J. Biomed. Mater. Res. A 67 (2003) 1115-22.
25. S. Haimi, G. Gorianc, L. Moimas, B. Lindroos, H. Huhtala, S.Raty, H. Kuokkanen, G.K. Sandor, C. Schmid, S. Miettinen, R. Suuronen, Characterization of zinc-releasing three-dimensional bioactive glass scaffolds and their effect on human adipose stem cell proliferation and osteogenic differentiation, Acta Biomater. 5 (2009) 3122.

26. Y. Jiang, J. Ou, Z. Zhang, Q.-H. Qin, Preparation of magnetic and bioactive calcium zinc iron silicon oxide composite for hyperthermia treatment of bone cancer and repair of bone defects, Journal of Materials Science: Materials in Medicine, 2011, 22 (3), pp. 721-72.
27. S.A: Shah, M.U. Hashmi, S. Alam, A. Shamim, Magnetic and bioactivity evaluation of ferrimagnetic ZnFe2O4 containing glass ceramics for the hyperthermia treatment of cancer, Journal of Magnetism and Magnetic Materials, 2010, 322 (3), pp. 375-381
28. C.J. Brinker, Hydrolysis and condensation of silicates, Journal of Non-Crystalline Solids 100 (1988) 31-50
29. D. Baciu, J. Simitzis, Synthesis and characterization of a calcium silicate bioactive glass, J. Optoelectron. Adv. Mater. (2007) 9 (11) 3320 – 3324.
30. M. Tamasan, T. Radu, S. Simon, I. Barbur, H. Mocuta, V. Simon, Thermal analysis of sol-gel aluminosilicate systems, J. Optoelectron. Adv. Mater. **10**, 948-950 (2008).
31. S. Simon, M. Tamasan, T. Radu, V. Simon, Doping and calcination effect on nanostructured aluminosilicates processed by sol-gel route, Eur. Phys. J. Appl. Phys. **55**, 30401 (2011)
32. C. Mirestean, P. Berce, S. Simon, Influence of heat treatment atmosphere on the superparamagnetic iron oxide – hydroxyapatite composites J. Optoelectron. Adv. Mater. 12, No. 9, September 2010, p. 1899 – 1902
33. L. Radev, V. Hristov, I. Michailova, B. Samuneva, Sol-gel bioactive glass-ceramics Part I: Calcium Phosphate Silicate/Wollastonite glass-ceramics,Cent. Eur. J. Chem. **7**, 317-321 (2009)
34. S.D. Conzone, D.E. Day, Preparation and properties of porous microspheres made from borate glass, J. Biomed. Mater. Res. A **88**, 531-542 (2009)
35. H. Masai, T. Toda, Y. Takahashi, T. Fujiwara, Fabrication of Bi-free TiO2 nano-crystallized glass, Journal of Non-Crystalline Solids 356 (2010) 2674–2676
36. **L. Pătcaş**, E. Vanea, M. Tămăşan, D. Eniu, V. Simon, Nanostructural changes induced by thermal treatment of calcium-silicate glasses containing dysprosium and iron, Optoelectronics and Advanced Materials – Rapid Communications, **8**, 989-992 (2014)
37. J.A. Curcio, C.C. Petty, The near infrared absorption spectrum of liquid water, J. Opt. Soc. Am. **41**, 302 (1951).
38. R.Schermaul, R.C.M. Learner, D.A. Newnham, R.G. Williams, J. Ballard, N.F. Zobov, D. Belmiloud, J. Tennyson, The water vapor spectrum in the region 8600-15

000 cm-1: Experimental and theoretical studies for a new spectral line database: I. Laboratory Measurements, J. Mol. Spectrosc. **208**, 32-42 (2001).

39. M. Kraken, I.-C. Masthoff, A. Borchers, F.J. Litterst, G. Garnweitner, Formation of magnetic nanoparticles studied during the initial synthesis stage, Hyperfine Interact. **224**, 57-63 (2014).
40. A. Martucci, N. Bassiri, M. Guglielmi, NiO-SiO_2 sol-gel nanocomposite films for optical gas sensor, J. Sol-Gel Sci. Techn. **26**, 993-996 (2003).
41. H. Zhang, G. Zhao, T. Zhang, F. Teng, Syntheses and photocatalytic performances of vertically grown Fe_2O_3 and TiO_2/Fe_2O_3 nanorods on coated glass substrates, J. Alloys Compd. 603 (2014) 35–41.
42. P.I.P. Soares, A.M.R. Alves, L.C.J. Pereira, J.T. Coutinho, I.M.M. Ferreira, C.M.M. Novo, J.P.M.R. Borges, Effects of surfactants on the magnetic properties of iron oxide colloids, J. Colloid Interf. Sci. 419 (2014) 46–51.
43. Y. Lv, K. Li, Y. Li, Surface modification of quantum dots and magnetic nanoparticles with PEG-conjugated chitosan derivatives for biological applications, Chem. Pap. **67**, 1404-1413 (2013).
44. A. Kumar, A. Singhal, Synthesis of colloidal β-Fe_2O_3 nanostructures - influence of addition of Co^{2+} on their morphology and magnetic behavior, Nanotechnology (2007), 18, 475703 (7pp).
45. F. Branda, A. Costantini, G. Luciani, B. Silvestri, Effect of changing the substituent oxide and its amount on the thermal stability towards crystallisation of glasses of formula (2·5-x)CaOx/3M2O3.2SiO2(M=La,Y,In,Ga) Physics and Chemistry of Glasses Part B (2004) 45 (2) pp.95-96.
46. K. N'Dri, D. Houphouet-Boigny, J.C. Jumas, J. Olivier-Fourcade, Electronegativity difference, atomic size parameter and widths of supercooled liquid regions of Sb2S3–As2S3–Sb2Te3 glasses, Journal of Non-Crystalline Solids 357 (2011) 145–149.
47. R.D. Shannon, Revised effective ionic radii and systematic studies of interatomic distances in halides and chalcogenides Acta Cryst. (1976) A32, 751-767.
48. J.E. Huheey, E.A. Keiter, R.L. Keiter, Inorganic Chemistry: Principles of Structure and Reactivity (4th Ed.)HarperCollins, New York, USA (1993)
49. J.A. Kerr, Strengths of chemical bonds**,** In**:**D.R. Lide (Ed.), CRC Handbook of Chemistry and Physics (81st Ed.), CRC Press, Boca Raton, FL, USA (2000
50. R.F.S. Lenza, W.L.Vasconcelos, Preparation of silica by sol-gel method using formamide, Materials Research, Vol. 4, No. 3, 189-194, 2001.

51. Saravanapavan, P., & L Hench, L. (2003). Mesoporous calcium silicate glasses. I. Synthesis, *Journal of non-crystalline solids*, 318 (1-2) pp. 1-13
52. A. R. Kuzmyn, A. de los Santos Pereira, O. Pop-Georgievski, M. Bruns, E. Brynda, C. Rodriguez-Emmenegger, Exploiting end group functionalization for the design of antifouling bioactive brushes, *Polym. Chem.*, 2014,5, 4124-4131
53. H. Zhang, K. Zhou, Z. Li, S. Huang, Synthesis of hollow hybrid hydroxyapatite microspheres based on chitosan–poly(acrylic acid) microparticles, Biomed. Mater. 4 (2009) 031002 (6pp)
54. M. A. Karakassides, D. Gournis, D. Petridis, An infrared reflectance study of Si-O vibrations in thermally treated alkalisaturated montmorillonites *Clay Minerals* (1999) 34,429-438.
55. R.L. Frost, S.J. Palmer, B.J. Reddy, (2007) Near-infrared and mid-IR spectroscopy of selected humite minerals. . *Vibrational Spectroscopy* 44(1):pp. 154-161
56. Marchi, J., Morais, D. S., Schneider, J., Bressiani, J. C., & Bressiani, A. H. A. (2005). Characterization of rare earth aluminosilicate glasses. *Journal of non-crystalline solids*, *351*(10), 863-868
57. Veres, R., Vanea, E., Gruian, C., Baia, L., & Simon, V. (2014). The effects of PEG assisted synthesis and zinc addition on gamma irradiated bioactive glasses. *Composites Part B: Engineering*, 66, pp. 83-88
58. M. Handke and W. Mozgawa, Vibrational spectroscopy of the amorphous silicates, Vibrational Spectroscopy,(1993) Vol. 5(1) 75
59. M. Mami, A. Lucas-Girot, H. Oudadesse, R. Dorbez-Sridi, F. Mezahi, E. Dietrich, Investigation of the surface reactivity of a sol–gel derived glass in the ternary system SiO2–CaO–P2O5, Applied Surface Science 254 (2008) 7386–7393
60. U. Anjaneyulu, S Sasikumar, Bioactive nanocrystalline wollastonite synthesized by sol–gel combustion method by using eggshell waste as calcium source, Bull. Mater. Sci. Vol. 37, No. 2, April 2014, pp. 207–212
61. R. K. Vempati, R. H. Loeppert, H. Sittertz-Bhatkar, R. C. Burghardt, Infrared vibrations of hematite formed from aqueous- and dry-thermal incubation of Si-containing ferrihydrite, *Clays and Clay Minerals*, Vol. 38, No. 3, 294-298, 1990
62. Sreekanth Chakradhar, R. P., Nagabhushana, B. M., Chandrappa, G. T., Ramesh, K. P., & Rao, J. L. (2006). Solution combustion derived nanocrystalline macroporous wollastonite ceramics. *Materials chemistry and Physics*, *95*(1), 169-175

63. Paluszkiewicz, C., Blażewicz, M., Podporska, J., & Gumuła, T. (2008). Nucleation of hydroxyapatite layer on wollastonite material surface: FTIR studies. *Vibrational Spectroscopy*, *48*(2), 263-268
64. T. Nishida, M. Suzuki, S. Kubuki, M. Katada, Y. Maeda, Occupation of tungsten site by iron in sodium tungstate glasses, J. Non-Cryst. Solids 194 (1996) 23-33
65. A. Roychowdhury, S.P. Pati, S. Kumar, D. Das, Effects of magnetite nanoparticles on optical properties of zinc sulfide in fluorescent-magnetic Fe_3O_4/ZnS nanocomposites, Powder Technology 254 (2014) 583–590
66. A. Hardy, C. Adelmann, S. Van Elshocht, H. Van den Rul, M.K. Van Bael, S. De Gendt, M. D'Olieslaeger, M. Heyns, J.A. Kittl, J. Mullens, Study of interfacial reactions and phase stabilization of mixed Sc, Dy, Hf high-k oxides by attenuated total reflectance infrared spectroscopy, Applied Surface Science 255 (2009) 7812–7817
67. V. Singh, S. Sharma, P.K. Jha, M. Kumar,R.K. Dwivedi, Effect of Y^{3+} substitute on structural, electrical and optical properties of $BiFeO_3$ ceramics, Ceram. Int. (2014) 40 (1B) 1971–1977.
68. I. Ardelean, M. Peteanu, V. Simon, F. Ciorcas, EPR and magnetic susceptibiliy investigations of Fe containing TeO_2-B_2O_3-SrF_2 glasses, J. Mat. Sci. Technol., 16, 6, 596-600 (2000)
69. S. Simon, R. Pop, V. Simon, M. Coldea, Structural and magnetic properties of lead-bismuthate oxide glasses containing S-state paramagnetic ions, J. Non-Cryst. Solids, 331, 1-3, 1-10 (2003)
70. N. Shankhwar, G.P.Kothiyal, A.Srinivasan, Understanding the magnetic behavior of heat treated CaO–P2O5–Na2O–Fe2O3–SiO2 bioactive glass using electron paramagnetic resonance studies, Physica B 448 (2014) 132–135
71. T. Castner Jr., G.S. Newell, W.C. Holtan, C.P. Slichter, Note on the paramagnetic resonance of iron in glass, J. Chem. Phys. 32 (1960) 668-673.
72. A. Murali, J.L. Rao, G.L. Narendra, Harinathudu, Electron paramagnetic resonance and optical absorption spectra of Fe(III) ions in lead acetate glasses, Opt. Mater. 7 (1997) 41-46.
73. R.P. Sreekanth Chakradhar, K.P. Ramesh, J.L. Rao, J. Ramakrishna, The effect of mixed alkali on EPR and optical absorption spectra in mixed alkali borate xNa2O–(30-x)K2O–70B2O3 glasses doped with iron ions, Journal of Non-Crystalline Solids 351 (2005) 1289–1299

74. F. Chavez-Rivas, G. Rodriguez-Fuentes, G. Berlier, I. Rodriguez-Iznaga, V. Petranovskii, R. Zamorano-Ulloa , S. Coluccia, Evidence for controlled insertion of Fe ions in the framework of clinoptilolite natural zeolites, Microporous and Mesoporous Materials 167 (2013) 76–81
75. P. Tartaj, M. del Puerto Morales, S. Veintemillas-Verdaguer, T. Gonzalez-Carreno, C.J. Serna, The preparation of magnetic nanoparticles for applications in biomedicine, J. Phys. D: Appl. Phys. **36** (2003) R182–R197
76. A. Espinosa, A. Serrano, A. Llavona, J. Jimenez de la Morena, M. Abuin, A Figuerola, T. Pellegrino, J.F. Fernandez, M. Garcia-Hernandez, G.R. Castro, M.A. Garcia, On the discrimination between magnetite and maghemite by XANES measurements in fluorescence mode, Meas. Sci. Technol. **23** (2012) 015602
77. D.L. Griscom, Ferromagnetic resonance of fine grained precipitates in glass: a thumbnail review, J. Non-Cryst. Solids, **42**, 287–296 (1980.).
78. A.U. Gehring, R. Karthein, An ESR and calorimetric study of iron oolitic samples from the Northampton Ironstone, Clay Miner. **25**, 303–311 (1990)
79. H. Fischer, J. Luster, A.U. Gehring, EPR evidence for maghemitization of magnetite in a tropical soil, Geophys. J. Int. **169,** 909–916 (2007)
80. D. Eniu, C. Gruian, E. Vanea, **L. Patcas**, V. Simon,' FTIR and EPR spectroscopic investigation of calcium-silicate glasses with iron and dysprosium, J. Mol. Struct. **1089**, 111-116 (2015).
81. E. Vanea, C. Gruian, **L. Pătcaş** , C.V. Moraru, V. Simon, Preliminary study regarding the biocompatibility of some new biomaterials designed for synergic hyperthermia/radioterapia applications, Studia UBB - Physica (2013) 58 (LVIII) 1, 67-76.
82. R. Ciceo Lucacel, O. Ponta, V. Simon, Short-range structure and in vitro behavior of ZnO–CaO–P2O5 bioglasses, J. Non-Cryst. Solids **358**, 2803-2809 (2012).
83. R. Veres, A. Vulpoi, K. Magyari, C. Ciuce, V. Simon,Synthesis, characterisation and **in vitro** testing of macroporous zinc containing scaffolds obtained by sol–gel and sacrificial template methods, J. Non-Cryst. Solids **373-374**, 57-64 (2013).